PHOTONICS Research

Second-harmonic generation and manipulation in lithium niobate slab waveguides by grating metasurfaces

Bin Fang,[1,2] Hanmeng Li,[1,2] Shining Zhu,[1,2] and Tao Li[1,2,*]

[1]National Laboratory of Solid State Microstructures, Key Laboratory of Intelligent Optical Sensing and Integration, Jiangsu Key Laboratory of Artificial Functional Materials, College of Engineering and Applied Sciences, Nanjing University, Nanjing 210093, China
[2]Collaborative Innovation Center of Advanced Microstructures, Nanjing 210093, China
*Corresponding author: taoli@nju.edu.cn

Received 11 March 2020; revised 9 May 2020; accepted 1 June 2020; posted 3 June 2020 (Doc. ID 391850); published 14 July 2020

Nonlinear optical processes in waveguides play important roles in compact integrated photonics, while efficient coupling and manipulations inside the waveguides still remain challenging. In this work, we propose a new scheme for second-harmonic generation as well as beam shaping in lithium niobate slab waveguides with the assistance of well-designed grating metasurfaces at $\lambda = 1064$ nm. By encoding the amplitude and phase into the holographic gratings, we further demonstrate strong functionalities of nonlinear beam shaping by the metasurface design, including dual focusing and Airy beam generation. Our approach would inspire new designs in the miniaturization and integration of compact multifunctional nonlinear light sources on chip.

https://doi.org/10.1364/PRJ.391850

1. INTRODUCTION

Since optical harmonic generation was first observed by Franken *et al.* [1] in a single-crystal quartz in 1961, nonlinear optics has achieved enormous developments, which have a wide range of significant applications in sensors [2], wavelength converters [3–5], optical frequency combs [6–8], all-optical signal processors [9], and quantum memories [10]. It is essential to strictly satisfy the phase-matching condition in order to ensure the continuously generated nonlinear optical waves can interfere with each other constructively. Generally, the phase-matching condition can be fulfilled by birefringent phase matching (BPM), quasi-phase matching (QPM), and cavity phase matching (CPM) [11]. Lithium niobate ($LiNbO_3$, LN) is an excellent material with outstanding optical properties including a high refractive index (~2.2 in the visible) enabling tight confinement of the optical field, a wide low-loss optical transparency window spanning from 350 nm to 5.2 μm, and large piezoelectric response and large electro-optic coefficient for optical modulators [12]. Most of all, it has large second-order nonlinear susceptibility (~27 pm/V) [12], which makes it a good material platform for nonlinear optical processes.

Despite LN's excellent linear and nonlinear optical properties, its intrinsic inert chemical properties and physical hardness have prevented the development of LN nanophotonics. Fortunately, inspired by the silicon-on-insulator (SOI) technology in the semiconductor industry, which has promoted the evolution of compact photonic integrated devices and circuits [13], $LiNbO_3$-on-insulator (LNOI) substrates have been commercially available in recent years. The LN thin film is located on top of the low-index SiO_2 buffer layer, fabricated via ion slicing and crystal bonding [14]. Due to the high refractive index contrast between $LiNbO_3$ and the substrate, it is efficient for confining the light into subwavelength scale and offers an opportunity for dense integrated devices. Since then, there has been encouraging progress in fabricating diverse thin-film LN optical devices [15–25]. In particular, LN nanowaveguides and their application in efficient nonlinear frequency conversions have been demonstrated, including modal phase matching between different waveguide modes [26–30], quasi-phase matching in periodically poled [31–33] or grooved [28] LN waveguides, phase-matching-free second-harmonic generation (SHG) assisted with phase gradient metasurfaces [34], and others. However, most of these works focus on the ridge waveguides, which are usually difficult to implement for beam shaping [35].

In this work, we experimentally demonstrate SHG as well as beam shaping in LN slab waveguides on a monolithic *z*-cut LNOI based on grating metasurfaces. Instead of using previous poling technology or precisely engineering the dispersion properties and geometric features of the waveguide, we directly fulfill the phase-matching condition via a simple grating metasurface that can implement the nonlinear process from the free-space fundamental wave to the guided second-harmonic (SH)

wave. Moreover, holographic designs are further introduced in the metasurface on the slab waveguide, which enables flexible nonlinear beam shaping. We experimentally demonstrated multifocusing and Airy beam SHG, promising multichannel nonlinear conversion and generation for optical interconnections.

2. DESIGN AND SIMULATIONS

In our study, the LNOI platform is employed with a single crystal z-cut LN thin-film layer with a thickness of 300 nm, underneath which is a 1.8 μm thick SiO_2 substrate. Owing to the high index contrast and the subwavelength thickness of the LN film, the waveguide modes are well confined into a small scale. The film is considered a slab waveguide in our scheme. As illustrated in Fig. 1(a), the $\lambda = 1064$ nm transverse-magnetic (TM) pump light is incident on the waveguide with a large incident angle of θ to the $-z$ direction from the free space (z is the LN extraordinary axis), and it mainly uses the d_{33} nonlinear coefficient. To achieve phase matching for SHG in the LN slab waveguide and guarantee that the SH intensity is accumulated constructively with the same phase, a simple grating metasurface is designed along the direction of propagation on the top surface of the waveguide. We performed oblique incidence in consideration of reducing the restrictions in fabrication of nanostructures with a small period. Since the slab waveguide supports both transverse-electric (TE) and TM modes, here we are more interested in the TM_0 mode of 532 nm. The phase-matching condition is given by

$$n_{\text{eff}} \cdot \frac{2\pi}{\lambda_{532}} = 2\frac{2\pi}{\lambda_{1064}} \sin\theta + m\frac{2\pi}{s}, \tag{1}$$

where n_{eff} is the effective index of the TM_0 guided mode of 532 nm, θ is the incident angle of the 1064 nm pump, m is the diffraction order (here $m = 1$), and s is the period of the gratings. The wave vector mismatch along the y axis between the target mode (β_{532}) and the pump ($k_{1064//}$) is compensated for by the lattice vector (G) of carefully designed gratings.

In principle, there are several parameters that can be optimized to access the phase-matching condition. Here we mainly want to provide a proof-of-concept demonstration and will not focus too much on parameter optimization. For simplicity, we fix several parameters. In detail, the grating period $s = 430$ nm, the duty cycle $D = 0.23$, the etching depth $h = 50$ nm, the length of the coupling region $L = 50$ μm, the width of the coupling region $W = 20$ μm, and thus the TM pump incident angle θ can be adjusted for the best phase-matching condition. Figure 1(b) shows the evolution of the electric field inside the slab waveguide at the SH frequency when $\theta = 58°$, obtained by the finite-difference time-domain (FDTD Solutions, Lumerical) simulations. The results demonstrate that the SH signal is well confined in the nanofilm slab waveguide, and it keeps accumulating throughout the grating-functioned region (highlighted with the pink box), indicating that the optical power is converted from the pump to the SH signal efficiently. Figure 1(c) displays the simulated SHG intensity evolutions in propagation with respect to different incident angle (θ). For either smaller or larger incident angles, there are considerable phase mismatches along the y direction, and thus the energy of the SH signals falls back into the coupling region. Only by approaching an appropriate angle ($\theta = 58°$) will the energy keep increasing rapidly. Besides, the sinc^2-function dependence of the SHG on the incident angle is also observed in Fig. 1(d), confirming the phase-matching condition.

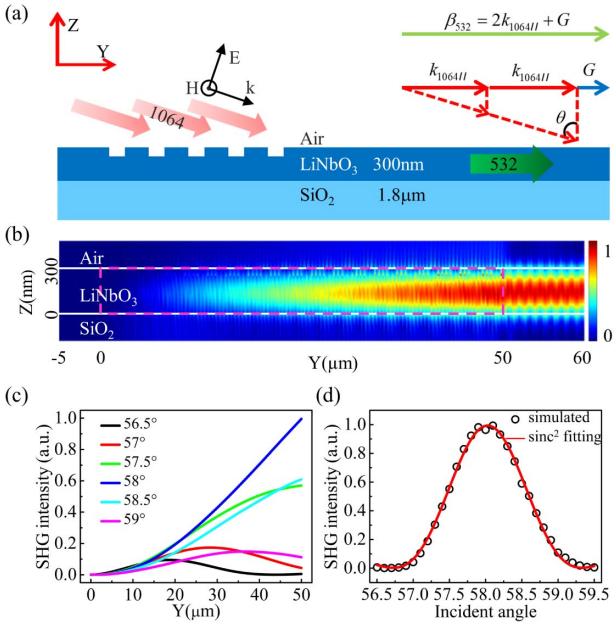

Fig. 1. Schematic illustration of the phase-matching process and the simulations. (a) Theoretical principle of the proposed SHG in the LN slab waveguide. (b) Simulated evolution of the electric field in the waveguide at the SH frequency, indicating an efficient SHG process. The grating distributed region is emphasized with the pink box. (c) Simulated SHG intensity versus propagation length with different incident angles θ. (d) Simulated sinc^2-dependence of the SHG on the incident angle.

3. FABRICATION AND MEASUREMENTS

In experiments, we fabricated the slab waveguides patterned with grating metasurfaces by a focused ion beam (FIB, dual-beam FEI Helios 600i) with acceleration voltage of 30 kV and beam current of 40 pA. Due to the poor electrical conductivity of LN, a 50 nm thick Ag layer was first deposited on the bare thin-film top surface via ion beam sputtering, and it was removed in dilute HNO_3 after the FIB etching. Figure 2(a) shows the scanning electron microscope (SEM) images of the fabricated structures before the Ag cladding was removed. The length of the coupling region patterned with gratings varied from 30, to 50, to 100 μm, while the width remained the same at 20 μm. The details of the gratings are shown in the zoom-in SEM image in Fig. 2(a). There is a facet diced 300 μm away from the structure's right side and polished by FIB in large beam current in order to guide the SH signals out.

A femtosecond laser with $\lambda = 1064$ nm (Fianium, pulse width of ~200 fs, repetition rate of 40 MHz) is employed for illumination with an incident angle of θ_i. A collection of an objective lens and a group of filters is placed before the

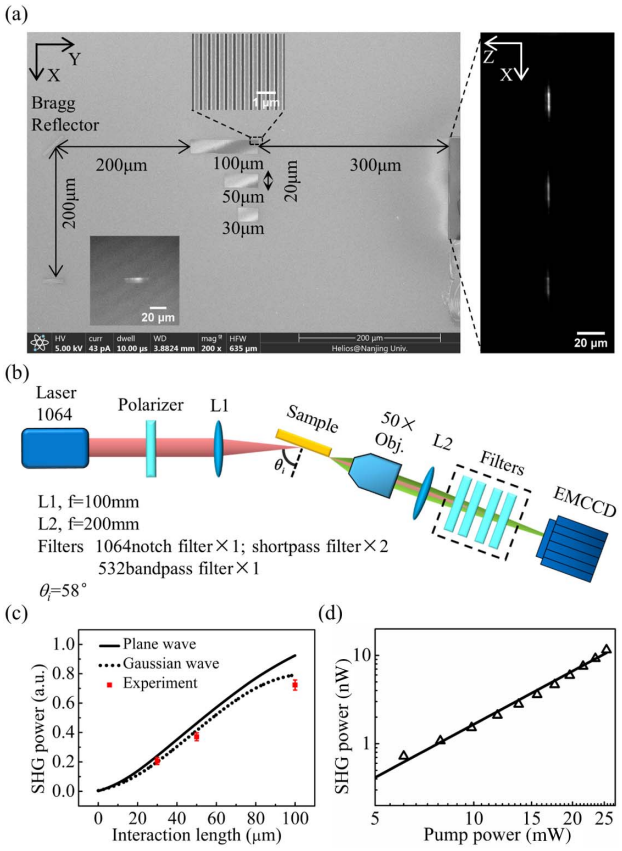

Fig. 2. Experimental demonstration of the SHG in the slab waveguide. (a) SEM images of the fabricated samples with Ag cladding. (b) Schematic illustration of the measurement setup. (c) Measured SHG power at the output port of samples with different lengths of the coupling regions, in comparison with the simulations. (d) Quadratic power dependence between the pump and the SH signal in the experiments.

electron multiplying charge coupled device (EMCCD, Andor, iXon Ultra 888) to detect the SHG signals as they are output from the waveguide's diced facet as in the optical setting shown in Fig. 2(b). The obliquely incident pumping light is slightly focused with an elliptical spot onto the center of each structure, whose dimensions are about 314 μm × 178 μm, which exceed the grating metasurface. The figure on the right side of Fig. 2(a) depicts the output spots of SH light (at 532 nm) generated via the waveguide coupling and nonlinear conversion from different length samples, which clearly exhibit different intensities. Figure 2(c) shows the measured SHG power (symbols) from these three waveguides compared with the simulation results (curves). For the ideal plane wave illumination illustrated by a black solid curve, we will see a quadratic increase of the SH power at the beginning as expected. However, for the longer conversion distance, the increase slows down, possibly due to the propagation loss of SH waves inside the waveguide with etched gratings. For the Gaussian beam pump, we are aware that the pumping spot should have nonuniform field intensity, which is much weaker at the edge. As a result, the increase of the SH power is even slower than the plane wave as the dotted curve shows in Fig. 2(c). In fact, our experimental data (red symbols) are consistent with the Gaussian beam simulations. Afterwards, we further measured the SHG power generated in the same waveguide ($L = 50$ μm) with different pump powers. The pump power is effectively averaged by the illumination with respect to the coupling region according to specific size, and a quadratic input–output power relation is obtained as shown in Fig. 2(d), confirming its second-order nonlinear process. According to our data, the total conversion efficiency is 4.6×10^{-7} for an average pump power of 25 mW.

In addition, to show the in-plane manipulation of the generated SH wave, we fabricated a 90°-turn reflection Bragg grating (period $s = 181$ nm with a 45° angle) to the left side of the 100 μm sample with a distance of 200 μm. Below this reflector, an out-of-plane grating coupler (period $s = 256$ nm) was made with a distance of 200 μm in the x direction. In this case, the 1064 nm light is incident with an opposite inclined angle (from right to left) onto the grating metasurfaces, and thus the SHG wave will propagate to the left direction. The generated 532 nm SH wave will be reflected by the Bragg reflector and propagate to x direction as in the coupled out signal shown in the inset figure [bottom left in Fig. 2(a)]. It definitely shows the function of the in-plane manipulation for the guided wave.

4. MANIPULATION OF THE SHG GUIDED WAVE

More importantly, our method offers a powerful tool in manipulating the wavefront of the SH signals inside the waveguide without extra devices. The two-dimensional hologram is encoded in the grating metasurfaces by the following equation [36,37]:

$$h(y,x) = \frac{h_0}{2}\left\{1 + \text{sign}\left\{\cos\left[\frac{2\pi}{s}y + \phi_i(x)\right] - \cos[\pi q(x)]\right\}\right\}. \quad (2)$$

This equation describes a binary modulated grating based on holographic technology, where $h_0 = 50$ nm is the etching depth of the grating, and $s = 430$ nm is the period in the direction of propagation y, which satisfies the phase-matching condition. $q = \arcsin[A(x)]/\pi$ where $A(x)$ contains the information of the amplitude, and $\phi_i(x)$ is the desired initial phase encoded in the transverse direction x in order to control the guided mode to follow a special trajectory in propagation.

According to the hologram design, we have fabricated another three samples by FIB with different SHG beam shaping functions (area of the coupling region of 50 μm × 20 μm). In detail, we obtain the desired phase and amplitude by holography. We consider the target wavefront as an object wave, and it interferes with the incident SHG plane wave. For multifocal lens designs, the holographic field of the sources in the x axis of gratings can be calculated by summarizing all the radiations from the focus as [38,39]

$$E(x) = \sum_n \frac{1}{\sqrt{r_n}} E_n \exp(ikr_n), \quad (3)$$

where r_n is the distance between the n_{th} focus and the source position in the x axis, and E_n is the amplitude of the n_{th} focus. For one focal lens ($f = 300$ μm) and dual focal lens (with distance of 50 μm) designs, we obtain the phase function and keep

the amplitude function $\cos[\pi q(x)]$ constant, which means the amplitude is uniform. In order to realize the Airy beam inside the waveguide, we use the following expression for the electric field distribution [40]:

$$E_{\mathrm{Airy}}(x) = \mathrm{Ai}\left(\frac{x}{x_0}\right). \tag{4}$$

Here Ai is the Airy function and x_0 is a transverse scaling factor, here chosen to be 2.048 μm for demonstration. The complex result of Eq. (4) can be separated into amplitude and phase terms, which in turn can be inserted into Eq. (2) to form the encoding pattern of the nonlinear Airy hologram.

Figures 3(a)–3(d) show the zoom-in SEM images of a part of the grating metasurfaces, and all these samples can convert the 1064 nm pump into 532 nm signals. The first one in Fig. 3(a) is just an ordinary case for a Gaussian beam, while those in Figs. 3(b) and 3(c) can perform as a one-focus or dual-focus in-plane lens, respectively, which promises applications in splitting the laser into multiple channels with a convenient and flexible routing method. The last one [see Fig. 3(d)] can generate nonlinear Airy beams inside the waveguide. Figures 3(e)–3(h) show the experimental results, and the corresponding vertical cross sections of the spots are also illustrated in Figs. 3(i)–3(l) with black solid curves. Additionally, we also performed a theoretical calculation based on the Huygens–Fresnel principle [41–43], in which nanostructures are considered as sub-sources radiating SH waves with designed initial phases. The calculated wavefront profiles [shown in Figs. 3(i)–3(l) with red dashed curves] are in good agreement with the experimental ones. The full widths at half –maxima (FWHMs) of the unfocused, single focused, and dual focused spots are 13.98, 3.25, 3.5, and 3.05 μm, respectively. The quality of the manipulated beam profiles is related to the fabrication and the accuracy realization of the amplitude as well as the phase. The total power of the generated SH signals for these samples slightly varies, which probably accounts for the different conversion efficiencies for different phase profiles.

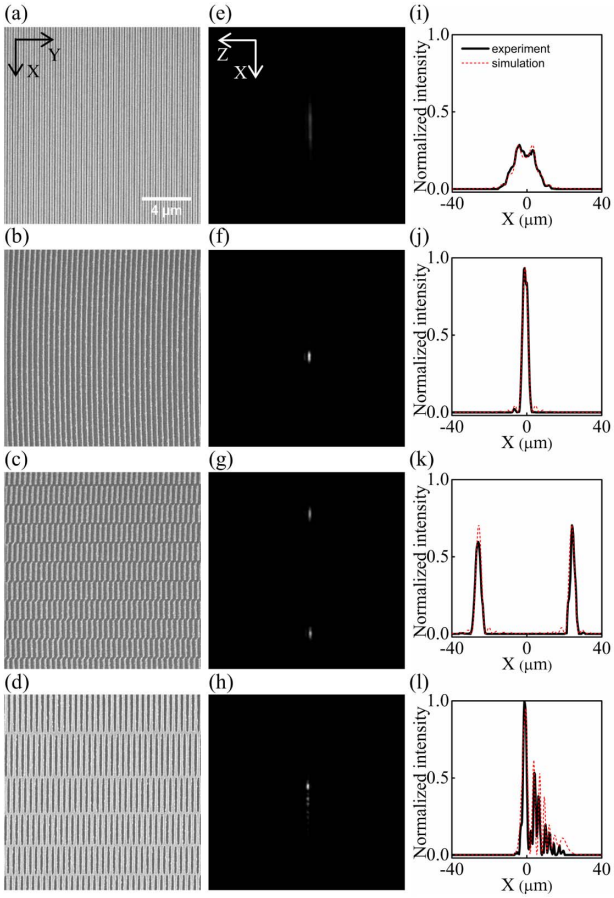

Fig. 3. Manipulation of SHG guided wave. Zoomed SEM images of structures for (a) an ordinary plane wave, (b) a focal lens, (c) a dual-focus lens, and (d) an Airy beam generator in the waveguide. (e)–(h) Measured light spot intensity profile coupling out from the facet of waveguides for four different beam manipulations. (i)–(l) Corresponding vertical cross sections of the light spots (black solid curves), in comparison with the simulation results (red dashed curves).

5. DISCUSSIONS AND CONCLUSION

Honestly speaking, the total efficiency of our approach is quite low as compared with previous works. However, it is reasonable since our approach merges several processes together, and the efficiency is not purely determined by the nonlinear conversion process within the waveguide. In our case, the fundamental wave is traveling in the free space with a certain efficiency to be coupled into a guided mode with a simultaneous nonlinear conversion, which indeed decreases the total efficiency remarkably. A possible solution to increase the coupling efficiency is to add a reflector below the slab-waveguide layer to capture more reflected pumping light, or even to construct a cavity in the vertical dimension to further enhance the interaction of incident light with the nanostructures.

In summary, we have demonstrated a new scheme to achieve nonlinear wavelength conversion and beam shaping in slab waveguides in the LNOI platform. With flexible grating metasurface designs, we convert the fundamental wave from free space into a manipulated guided SH wave, instead of the previous two or more steps, making the system simpler and more compact. Furthermore, the holographic grating metasurfaces enable us to manipulate the generated SH signals with one more degree of freedom, and we can control their wavefront in the waveguide as desired. Thus, we also demonstrated several functions in nonlinear beam shaping, like focusing, dual focusing, and the Airy beam generation, which offer opportunities for flexible on-chip multichannel routing. Our approach is promising to enable new exciting possibilities in integrated nonlinear nanophotonic designs and devices.

Funding. National Key Research and Development Program of China (2017YFA0303701, 2016YFA0202103); National Natural Science Foundation of China (11674167, 91850204).

Acknowledgment. T. Li is grateful for the support of Dengfeng Project B of Nanjing University.

Disclosures. The authors declare no conflicts of interest.

REFERENCES

1. P. A. Franken, A. E. Hill, C. W. Peters, and G. Weinreich, "Generation of optical harmonics," Phys. Rev. Lett. **7**, 118–119 (1961).
2. F. Vollmer and S. Arnold, "Whispering-gallery-mode biosensing: label-free detection down to single molecules," Nat. Methods **5**, 591–596 (2008).
3. E. J. Lim, M. M. Fejer, and R. L. Byer, "Second-harmonic generation of green light in periodically poled planar lithium niobate waveguide," Electron. Lett. **25**, 174–175 (1989).
4. J. P. Meyn, C. Laue, R. Knappe, R. Wallenstein, and M. M. Fejer, "Fabrication of periodically poled lithium tantalate for UV generation with diode lasers,"Appl. Phys. B **73**, 111–114 (2001).
5. K. L. Vodopyanov, M. M. Fejer, X. Yu, J. S. Harris, Y. S. Lee, W. C. Hurlbut, V. G. Kozlov, D. Bliss, and C. Lynch, "Terahertz-wave generation in quasi-phase-matched GaAs," Appl. Phys. Lett. **89**, 141119 (2006).
6. R. Holzwarth, T. Udem, T. W. Hansch, J. C. Knight, W. J. Wadsworth, and P. St. J. Russell, "Optical frequency synthesizer for precision spectroscopy," Phys. Rev. Lett. **85**, 2264–2267 (2000).
7. T. Udem, R. Holzwarth, and T. W. Hänsch, "Optical frequency metrology," Nature **416**, 233–237 (2002).
8. P. Del'Haye, A. Schliesser, O. Arcizet, T. Wilken, R. Holzwarth, and T. J. Kippenberg, "Optical frequency comb generation from a monolithic microresonator," Nature **450**, 1214–1217 (2007).
9. A. E. Willner, O. F. Yilmaz, J. Wang, X. Wu, A. Bogoni, L. Zhang, and S. R. Nuccio, "Optically efficient nonlinear signal processing," IEEE J. Sel. Top. Quantum Electron. **17**, 320–332 (2011).
10. N. Sinclair, E. Saglamyurek, H. Mallahzadeh, J. A. Slater, M. George, R. Ricken, M. P. Hedges, D. Oblak, C. Simon, W. Sohler, and W. Tittel, "Spectral multiplexing for scalable quantum photonics using an atomic frequency comb quantum memory and feed-forward control," Phys. Rev. Lett. **113**, 053603 (2014).
11. J. A. Armstrong, N. Bloembergen, J. Ducuing, and P. S. Pershan, "Interactions between light waves in a nonlinear dielectric," Phys. Rev. **127**, 1918–1939 (1962).
12. D. N. Nikogosyan, *Nonlinear Optical Crystals: A Complete Survey* (Springer, 2005).
13. B. Jalali and S. Fathpour, "Silicon photonics," J. Lightwave Technol. **24**, 4600–4615 (2006).
14. G. Poberaj, H. Hu, W. Sohler, and P. Günter, "Lithium niobate on insulator (LNOI) for micro-photonic devices," Laser Photon. Rev. **6**, 488–503 (2012).
15. C. Wang, M. J. Burek, Z. Lin, H. A. Atikian, V. Venkataraman, I. C. Huang, P. Stark, and M. Lončar, "Integrated high quality factor lithium niobate microdisk resonators," Opt. Express **22**, 30924–30933 (2014).
16. J. Lin, Y. Xu, Z. Fang, M. Wang, N. Wang, L. Qiao, W. Fang, and Y. Cheng, "Second harmonic generation in a high-Q lithium niobate microresonator fabricated by femtosecond laser micromachining," Sci. China Phys. Mech. Astron. **58**, 114209 (2015).
17. M. Zhang, C. Wang, R. Cheng, A. Shams-Ansari, and M. Lončar, "Monolithic ultra-high-Q lithium niobate microring resonator," Optica **4**, 1536–1537 (2017).
18. R. Wolf, Y. Jia, S. Bonaus, C. S. Werner, S. J. Herr, I. Breunig, K. Buse, and H. Zappe, "Quasi-phase-matched nonlinear optical frequency conversion in on-chip whispering galleries," Optica **5**, 872–875 (2018).
19. R. Wu, J. Zhang, N. Yao, W. Fang, L. Qiao, Z. Chai, J. Lin, and Y. Cheng, "Lithium niobate micro-disk resonators of quality factors above 10^7," Opt. Lett. **43**, 4116–4119 (2018).
20. C. Wang, M. Zhang, X. Chen, M. Bertrand, A. Shams-Ansari, S. Chandrasekhar, P. Winzer, and M. Lončar, "Integrated lithium niobate electro-optic modulators operating at CMOS-compatible voltages," Nature **562**, 101–104 (2018).
21. M. He, M. Xu, Y. Ren, J. Jian, Z. Ruan, Y. Xu, S. Gao, S. Sun, X. Wen, L. Zhou, L. Liu, C. Guo, H. Chen, S. Yu, L. Liu, and X. Cai, "High-performance hybrid silicon and lithium niobate Mach-Zehnder modulators for 100 Gbit s^{-1} and beyond," Nat. Photonics **13**, 359–364 (2019).
22. X. Wang, P. O. Weigel, J. Zhao, M. Ruesing, and S. Mookherjea, "Achieving beyond-100-GHz large-signal modulation bandwidth in hybrid silicon photonics Mach Zehnder modulators using thin film lithium niobate," APL Photon. **4**, 096101 (2019).
23. M. Xu, W. Chen, M. He, X. Wen, Z. Ruan, J. Xu, L. Chen, L. Liu, S. Yu, and X. Cai, "Michelson interferometer modulator based on hybrid silicon and lithium niobate platform," APL Photon. **4**, 100802 (2019).
24. M. Zhang, B. Buscaino, C. Wang, A. Shams-Ansari, C. Reimer, R. Zhu, J. M. Kahn, and M. Lončar, "Broadband electro-optic frequency comb generation in a lithium niobate microring resonator," Nature **568**, 373–377 (2019).
25. D. Pohl, M. R. Escalé, M. Madi, F. Kaufmann, P. Brotzer, A. Sergeyev, B. Guldimann, P. Giaccari, E. Alberti, U. Meier, and R. Grange, "An integrated broadband spectrometer on thin-film lithium niobate," Nat. Photonics **14**, 24–29 (2019).
26. R. Geiss, S. Saravi, A. Sergeyev, S. Diziain, F. Setzpfandt, F. Schrempel, R. Grange, E.-B. Kley, A. Tünnermann, and T. Pertsch, "Fabrication of nanoscale lithium niobate waveguides for second-harmonic generation," Opt. Lett. **40**, 2715–2718 (2015).
27. L. Cai, Y. Wang, and H. Hu, "Efficient second harmonic generation in $\chi^{(2)}$ profile reconfigured lithium niobate thin film," Opt. Commun. **387**, 405–408 (2017).
28. C. Wang, X. Xiong, N. Andrade, V. Venkataraman, X. Ren, G. Guo, and M. Lončar, "Second harmonic generation in nano-structured thin-film lithium niobate waveguides," Opt. Express **25**, 6963–6973 (2017).
29. R. Luo, Y. He, H. Liang, M. Li, and Q. Lin, "Highly tunable efficient second-harmonic generation in a lithium niobate nanophotonic waveguide," Optica **5**, 1006–1011 (2018).
30. R. Luo, Y. He, H. Liang, M. Li, and Q. Lin, "Semi-nonlinear nanophotonic waveguides for highly efficient second-harmonic generation," Laser Photon. Rev. **13**, 1800288 (2019).
31. L. Chang, Y. Li, N. Volet, L. Wang, J. Peters, and J. E. Bowers, "Thin film wavelength converters for photonic integrated circuits," Optica **3**, 531–535 (2016).
32. A. Rao, M. Malinowski, A. Honardoost, J. R. Talukder, P. Rabiei, P. Delfyett, and S. Fathpour, "Second-harmonic generation in periodically-poled thin film lithium niobate wafer-bonded on silicon," Opt. Express **24**, 29941–29947 (2016).
33. C. Wang, C. Langrock, A. Marandi, M. Jankowski, M. Zhang, B. Desiatov, M. M. Fejer, and M. Lončar, "Ultrahigh-efficiency wavelength conversion in nanophotonic periodically poled lithium niobate waveguides," Optica **5**, 1438–1441 (2018).
34. C. Wang, Z. Li, M. Kim, X. Xiong, X. Ren, G. Guo, N. Yu, and M. Lončar, "Metasurface-assisted phase-matching-free second harmonic generation in lithium niobate waveguides," Nat. Commun. **8**, 2098 (2017).
35. A. Boes, B. Corcoran, L. Chang, J. Bowers, and A. Mitchell, "Status and potential of lithium niobate on insulator (LNOI) for photonic integrated circuits," Laser Photon. Rev. **12**, 1700256 (2018).
36. W. H. Lee, "Binary computer-generated holograms," Appl. Opt. **18**, 3661–3669 (1979).
37. I. Dolev, I. Epstein, and A. Arie, "Surface-plasmon holographic beam shaping," Phys. Rev. Lett. **109**, 203903 (2012).
38. J. Chen, L. Li, T. Li, and S. N. Zhu, "Indefinite plasmonic beam engineering by in-plane holography," Sci. Rep. **6**, 28926 (2016).
39. C. Zhao, J. Chen, H. Li, T. Li, and S. Zhu, "Mode division multiplexed holography by out-of-plane scattering of plasmon/guided modes," Chin. Opt. Lett. **16**, 070901 (2018).
40. I. Epstein, Y. Lilach, and A. Arie, "Shaping plasmonic light beams with near-field plasmonic holograms," J. Opt. Soc. Am. B **31**, 1642–1647 (2014).
41. L. Li, T. Li, S. M. Wang, C. Zhang, and S. N. Zhu, "Plasmonic Airy beam generated by in-plane diffraction," Phys. Rev. Lett. **107**, 126804 (2011).
42. L. Li, T. Li, S. M. Wang, and S. N. Zhu, "Collimated plasmon beam: nondiffracting versus linearly focused," Phys. Rev. Lett. **110**, 046807 (2013).
43. Q. Q. Cheng, T. Li, L. Li, S. M. Wang, and S. N. Zhu, "Mode division multiplexing in a polymer-loaded plasmonic planar waveguide," Opt. Lett. **39**, 3900–3902 (2014).